Topological Superconductivity Based on Antisymmetric Spin−Orbit Coupling

Xiaoming Zhang,*,§ Jiale Liu,§ and Feng Liu*
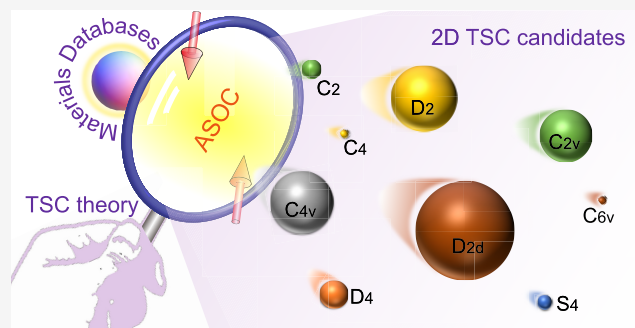
Read Online

ACCESS | Metrics & More | Article Recommendations | Supporting Information

ABSTRACT: Topological superconductivity (TSC) has drawn much attention for its fundamental interest and application in quantum computation. An outstanding challenge is the lack of intrinsic TSC materials with a p-wave pairing gap, which has led to the development of an effective p-wave theory of coupling s-wave gap with Rashba spin−orbit coupling (RSOC). However, the RSOC-strict mechanism and materials pose still both fundamental and practical limitations. Here, we generalize this theory to antisymmetric SOC (ASOC). Using $\mathbf{k}\cdot\mathbf{p}$ perturbation theory, we demonstrate that 2D crystals, with point groups of C_2, C_4, C_6, C_{2v}, C_{4v}, C_{6v}, D_2, D_4, D_6, S_4, or D_{2d}, can all facilitate the desired ASOC. Remarkably, this enables us to discover 314 TSC candidates by screening 2D material databases, which are further confirmed by first-principles calculations of Majorana boundary modes and the topological invariant of the superconducting gap. Our work fundamentally enriches TSC theory and greatly expands the classes of TSC materials for experimental exploration.

Topological superconductivity (TSC) is characterized by gapless Majorana boundary modes (MBMs) within the pairing gap of bulk states.[1−3] The nonabelian statistics of Majorana Fermions hosted by chiral MBMs[4−6] make the TSC promising candidates for fault-tolerant quantum computation.[7,8] A chiral TSC phase features an odd-parity pairing state on Fermi surface (FS) contours that enclose time-reversal-invariant momenta (TRIM). As the simplest odd-parity pairing, spin-triplet p-wave pairing naturally endows an intrinsic chiral TSC phase,[9,10] but it suffers from a severe limitation of material availability. This has motivated the proposal of extrinsic chiral TSC phase with an effective p-wave paring by conspiring the effects of s-wave superconductivity, Rashba spin−orbit coupling (RSOC), and Zeeman field,[11−14] which has been successfully realized in a few materials.[1−3,15−18] However, the condition of RSOC appears to be strict, which poses still a fundamental limitation on the physical mechanism of TSC as well as a practical limitation on the availability of RSOC materials. Here, we generalize this effective TSC theory to generic forms of antisymmetric SOC (ASOC), which greatly enriches the theory and enables us to identify over 300 candidate two-dimensional (2D) TSC materials.

The RSOC splits the bands into two spin branches in momentum space except at the TRIM protected by time-reversal-symmetry (TRS),[19,20] which creates two FS contours of opposite helical in-plane spin textures for each band. When an s-wave pairing condenses around the energy of Kramers pair (KP) at TRIM, an effective p-wave pairing gap would open on

both FS contours but with opposite chirality. By applying a Zeeman field to lift the spin degeneracy of KP, one can preserve the effective p-wave gap of one chirality for a given chemical potential,[11,21,22] thus enabling an extrinsic chiral TSC phase. One notices that the key to this TSC mechanism is to generate effective odd-parity pairing states in odd number of FS contours enclosing the TRIM, which is naturally satisfied for the RSOC bands under a Zeeman field. Importantly, we have realized that the helical spin texture on FS is only a sufficient but not mandatory condition because the s-wave pairing gap can still open on the FS as long as the electron spins are subjected to TRS, i.e., opposite spin orientations for electrons at k and $-k$, respectively. This significantly relaxed condition can be generally satisfied with any form of ASOC.

In general, ASOC originates from inversion-asymmetry-induced electric field gradient, so that electrons experience a momentum-dependent effective magnetic field without breaking TRS. The field lifts the band degeneracy and induces diverse patterns of spin texture around the KP at TRIM. Spin texture has been a focused research topic in the field of
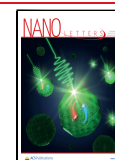
spintronics; in particular, a persistent spin texture is useful in the application of nonvolatile spintronic devices due to its extraordinarily long spin lifetime.[23−27] Meanwhile, the concepts of Kramers−Weyl semimetal[28] and Kramers nodal-line metal[29] were proposed by analyzing the KP and its associated spin texture, pointing to the diverse effects of ASOC. Interestingly, we reveal another fascinating effect of ASOC for generating TSC.

There are three basic forms of ASOC. One is the aforementioned RSOC, whose helical in-plane spin texture (see Figure 1a) results from an effective magnetic field in the
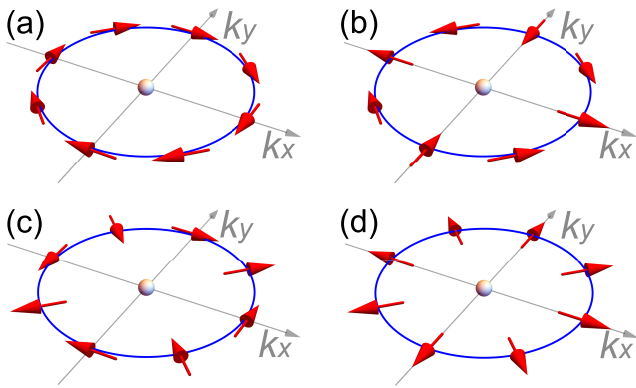

Figure 1. Schematic spin texture of four basic forms of ASOC on the FS contour around a KP (white dot). (a) RSOC, (b) DSOC, (c) D′SOC, and (d) WSOC.

form of $\lambda_R(k_x\sigma_y - k_y\sigma_x)$. RSOC originates from planar inversion (mirror) asymmetry, which can arise naturally at surface or interface,[30] in 2D materials[31,32] and thin films on a substrate.[33,34] Another well-known ASOC is the Dresselhaus SOC enabled by bulk inversion asymmetry,[35] which usually exists in bulk materials but can emerge also at 2D limit, such as quantum wells.[23] The effective field takes the form of $\lambda_D(k_x\sigma_x - k_y\sigma_y)$ or $\lambda_{D'}(k_x\sigma_x + k_y\sigma_x)$, which we abbreviate respectively as DSOC and D′SOC for the associated Dresselhaus SOC. Their spin orientations are relatively rotated by 90° at every $\boldsymbol{k}$-point in Figure 1 part b versus part c. Moreover, the KP of Weyl Fermions has been revealed in 2D chiral crystals.[36,37] The underlying Weyl SOC (WSOC) has an effective field form of $\lambda_W(k_x\sigma_x + k_y\sigma_y)$, which induces a radial spin texture (see Figure 1d). The spin texture patterns can be further enriched by a linear combination of the effective fields of RSOC, DSOC, D′SOC, and WSOC. For example, quantum wells are ideal platforms to combine RSOC with D′SOC or DSOC,[38,39] where the relative contribution of each[40] and the sign of $\lambda_{D/R}$[41,42] can vary with electric field. The combination between RSOC and WSOC can be made in ferroelectric hetero-structure.[43] This points to the possibility of inducing TSC phase in real materials with a generic form of ASOC, featured with arbitrary TRS-protected in-plane spin texture, which is highly intriguing and attractive.

In this Letter, we have carried out theoretical analysis and numerical calculations to demonstrate that a chiral TSC phase can be generally induced from any form of ASOC, whose effective magnetic field maintains an in-plane antiparallel spin orientation at $\boldsymbol{k}$ and $-\boldsymbol{k}$ on the FS contour enclosing a KP. The in-plane spin texture is protected by TRS, providing the precondition for maintaining an s-wave pairing gap Δ under an out-of-plane Zeeman field (Z). The transition point for the

TSC phase is same as that of RSOC,[11−14] i.e. $\sqrt{\Delta^2 + \mu^2} = Z$ (μ is chemical potential in reference to the energy of KP). We employ the $\boldsymbol{k}\cdot\boldsymbol{p}$ perturbation theory to analyze the symmetry-allowed effective fields of ASOC, which shows that the desired in-plane spin textures can be found in the 2D non-centrosymmetric crystals with the point group (PG) of C_2, C_4, C_6, C_{2v}, C_{4v}, C_{6v}, D_2, D_4, D_6, S_4, and D_{2d}. Remarkably, this enables us to discover 314 TSC candidates by screening the material databases of the 2D Materials Encyclopedia (2DMP)[44] and the Computational 2D Materials Database (C2DB).[45]

■ A GENERALIZED CHIRAL TSC MODEL

We recall the nonabelian topological order in the s-wave superfluid reported by Sato et al.,[11] who showed that the Bogoliubov−de Gennes (BdG) Hamiltonian $\mathcal{H}_{BdG}(\boldsymbol{k})$ with an s-wave pairing $i\Delta\sigma_y$ is equivalent to a 'dual' Hamiltonian $\mathcal{H}^D(\boldsymbol{k})$ with a pairing of $-i\boldsymbol{g}(\boldsymbol{k})\cdot\boldsymbol{\sigma}\sigma_y$ by a unitary trans-formation. Here the $\boldsymbol{g}(\boldsymbol{k})\cdot\boldsymbol{\sigma}$ is actually the RSOC term in $\mathcal{H}_{BdG}(\boldsymbol{k})$ with $\boldsymbol{g}(\boldsymbol{k}) = (-k_y, k_x)$ and $\boldsymbol{\sigma} = (\sigma_x, \sigma_y)$. By comparing with the p-wave pairing of $i\boldsymbol{d}(\boldsymbol{k})\cdot\boldsymbol{\sigma}\sigma_y$ with $\boldsymbol{d}(\boldsymbol{k}) = -\boldsymbol{d}(-\boldsymbol{k})$,[2] one immediately realizes that the pairing in $\mathcal{H}^D(\boldsymbol{k})$ can be effectively viewed as the p-wave pairing if $-\boldsymbol{g}(\boldsymbol{k})$, which satisfies $\boldsymbol{g}(\boldsymbol{k}) = -\boldsymbol{g}(-\boldsymbol{k})$, is regarded as $\boldsymbol{d}(\boldsymbol{k})$. Notably, the chirality of the effective p-wave pairing is opposite for the RSOC induced two FS contours due to the opposite helical spin texture, which will cancel each other out. The emergence of the TSC phase needs one of them to be removed by tuning the chemical potential and opening a Zeeman gap in the KP.[11,21,22]

Importantly, one can generalize the above arguments from RSOC to DSOC, D′SOC, and WSOC, because their effective fields are unitary equivalent with each other:

$$U_{RW}(k_x\sigma_x + k_y\sigma_y) = (k_x\sigma_y - k_y\sigma_x)U_{RW}, \text{ with } U_{RW} = \begin{pmatrix} i & 0 \\ 0 & 1 \end{pmatrix}$$
(1)

$$U_{WD}(k_x\sigma_x - k_y\sigma_y) = (k_x\sigma_x + k_y\sigma_y)U_{WD}, \text{ with } U_{WD} = \begin{pmatrix} \dfrac{k_x + ik_y}{k_x - ik_y} & 0 \\ 0 & 1 \end{pmatrix}$$
(2)

$$U_{RD'}(k_x\sigma_y + k_y\sigma_x) = (k_x\sigma_y - k_y\sigma_x)U_{RD'}, \text{ with } U_{RD'} = \begin{pmatrix} \dfrac{k_y + ik_x}{k_y - ik_x} & 0 \\ 0 & 1 \end{pmatrix}$$
(3)

The $\boldsymbol{d}(\boldsymbol{k})$ vector of effective odd-parity pairing induced by DSOC, D′SOC, and WSOC is respectively $(k_x, -k_y)$, (k_y, k_x), and (k_x, k_y), which are all antisymmetric and satisfy $\boldsymbol{d}(\boldsymbol{k}) = -\boldsymbol{d}(-\boldsymbol{k})$.

Furthermore, a linear combination of RSOC, DSOC, D′SOC, and WSOC will lead to a mixed SOC having the antisymmetric $\boldsymbol{d}(\boldsymbol{k})$ vector of $(\sum_{\alpha=x,y}\zeta_\alpha k_\alpha, \sum_{\beta=x,y}\eta_\beta k_\beta)$. Despite an overall "arbitrary" in-plane spin texture, antiparallel spin orientation for the electrons at $\boldsymbol{k}$ and $-\boldsymbol{k}$ is still preserved by the mixed SOC, which ensures the precondition for maintaining an s-wave pairing gap. Accordingly, the s-wave pairing can be effectively regarded as an odd-parity pairing because $\boldsymbol{d}(\boldsymbol{k})$ is of an odd power of momentum for any mixed SOC, albeit not in the standard p-waveform.

We have confirmed numerically the above analysis by constructing a tight-binding (TB) model in Section I of Supporting Information. Our calculations show that the TSC phase indeed emerges under the condition $\sqrt{\Delta^2 + \mu^2} < |Z|$ for the KP surrounded with arbitrary in-plane spin texture of any ASOC. This condition is the same as that of RSOC, since the TSC phase transition is only relevant to gap closing and reopening at TRIM, where the effective field vanishes, irrelevant to a specific form of ASOC.

We emphasize that this generalized mechanism of TSC is always valid around an isolated KP, which may exist in the candidate materials of single or multiple bands. In the latter case, the TSC phase can emerge by opening a pairing gap on an odd number of FS contours under proper chemical potential and Zeeman field. Two FSs manifesting an effective odd-parity pairing with opposite chirality will pairwise cancel out each other, so that one last FS contour will be left to enable the TSC phase. Consequently, one needs only to find an isolated KP surrounded with in-plane spin texture during screening TSC candidates, without distinguishing if it is a single-band or multiband system. Notably, this mechanism does not apply to nonisolated KPs connected by doubly degenerated nodal line under certain conditions, e.g. $\lambda_D = \lambda_W$, $\lambda_{D'} = \lambda_W$, $\lambda_D = \lambda_R$, and $\lambda_{D'} = \lambda_R$. This is because an s-wave gap cannot be opened on the nodal line when its degeneracy is lifted by the Zeeman field, as the electrons have the same spin orientation in the spin-polarized band at k and $-k$, violating TRS.

■ CHIRAL TSC CANDIDATE MATERIALS

Guided by our newly developed generalized theory of chiral TSC, we have carried out an extensive search of TSC candidate materials. We first perform a **k·p** analysis to derive the form of symmetry-allowed SOC Hamiltonian[46,47] based on the character table of PG.[48] For a 2D crystal in the x−y plane, σ_z must be zero to maintain an in-plane spin texture. Since k_z is not a good quantum number, this requirement is met when σ_z and $k_{x/y}$ are not sorted out simultaneously from the irreducible representation. Among the 21 noncentrosymmetric PGs, we found 11 to meet this requirement at the limit of 2D crystals with C_n rotational axis normal to the x−y plane, which are summarized in Table 1. The derived **k·p** Hamiltonian clearly indicates that a wide variety of ASOC, including RSOC, DSOC, WSOC, Rashba−Weyl SOC (RWSOC), Dresselhaus−Weyl SOC (DWSOC), Rashba−Dresselhaus SOC (RD′SOC), Dresselhaus−Dresselhaus SOC (DD′SOC), and Rashba−Dresselhaus−Dresselhaus−Weyl SOC (RDD′WSOC), can be

realized by C_{4v} or C_{6v}, D_{2d}, D_4 or D_6, C_4 or C_6, C_{2v}, D_2, S_4, and C_2 PG symmetry, respectively.

One can describe the spin texture around the KP by selecting the **k·p** Hamiltonian with the PG being identical with the little group of corresponding TRIM. Referring to the Web site of Bilbao Crystallographic Server,[49] we summarize the little group of TRIM (see Section II of the Supporting Information) for 92 noncentrosymmetric space groups (SGs) that belong to the 11 PGs. There are 14 different little groups for the TRIM in the 2D Brillouin zone within the k_x−k_y plane, including the 11 PGs listed in Table 1 and additional C_3, C_{3v}, and D_3 PGs. The linear term of k in the **k·p** Hamiltonian for the C_3, C_{3v}, and D_3 symmetry possesses RWSOC, RSOC, and WSOC form, respectively.

Next, candidate materials are searched from the material databases of 2DMP[44] and C2DB.[45] From 6351 2D materials in 2DMP and 1616 ones in C2DB, we screened out 1069 with the SGs that belong to the desired 11 PGs, and 857 of them are protected by TRS. Then, by selecting the materials with an out-of-plane C_n axes as for 2D symmetry groups, we finally identify 314 2D TSC candidates (see Figure 2a). Among them,
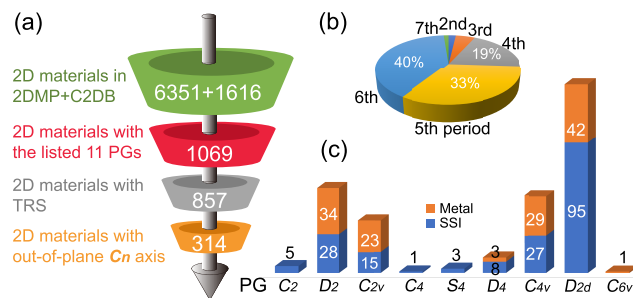

Figure 2. Illustration of screening candidate 2D TSC materials. (a) Procedure of screening the databases of 2DMP and C2DB. (b) Percentage of TSC materials whose heaviest element belongs to the 2nd-, 3rd-, 4th-, 5th-, 6th-, and 7th-period, respectively. (c) Distribution of TSC candidate materials among different PGs.

73% contains fifth- and sixth-period elements (see Figure 2b), and their strong SOC strength are beneficial to enable robust TSC against the Zeeman field. They are distributed among 9 PGs (see Figure 2c); nearly half of them belong to D_{2d} PG, and none belong to C_6 or D_6 PG. We then calculated the electronic band structure and spin texture of 314 candidates using first-principles method (see Section III of the Supporting Information). The list of screened candidates and the calculated results are summarized in Section IV of the Supporting Information. 132 materials are identified as metals and others are semimetal, semiconductor, or insulator (SSI), whose distributions are shown in Figure 2c. Notably, we found that the isolated KP emerges near the Fermi level for most of metallic candidates, suitable for realizing TSC phase without doping. For the SSI candidates, doping is needed to move the Fermi level to the energy of KP at TRIM.

Among all the TSC candidates with D_{2d} PG symmetry (see Figure 2c), more than 84% have the SG of $P\bar{4}m2$. Without losing generality, below we take $TaSe_2$ with this SG as a representative for discussion. $TaSe_2$ is constructed from the corner-sharing tetrahedral Se motifs with a Ta at the center (see Figure 3a), forming a 2D tetragonal lattice. As expected for symmorphic SGs, band degeneracies are removed by an ASOC at all the k points except the TRIM, ensuring isolated

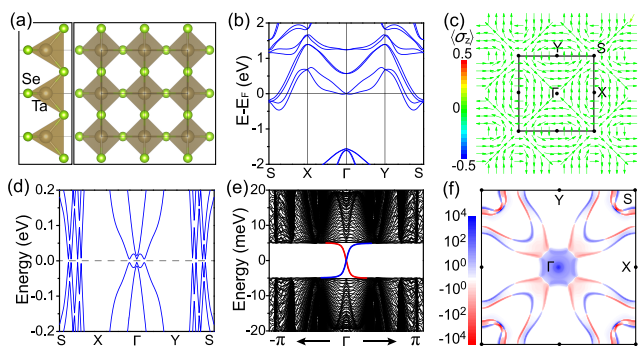**Table 1. 11 PGs and Associated k·p Hamiltonian That Enable the ASOC with In-Plane Spin Texture**

PG	k·p Hamiltonian	ASOC type
C_2	$\lambda_R(k_x\sigma_y - k_y\sigma_x) + \lambda_D(k_x\sigma_x - k_y\sigma_y)$ $+ \lambda_{D'}(k_x\sigma_y + k_y\sigma_x) + \lambda_W(k_x\sigma_x + k_y\sigma_y)$	RDD′WSOC
C_4, C_6	$\lambda_R(k_x\sigma_y - k_y\sigma_x) + \lambda_W(k_x\sigma_x + k_y\sigma_y)$	RWSOC
C_{2v}	$\lambda_R(k_x\sigma_y - k_y\sigma_x) + \lambda_{D'}(k_x\sigma_y + k_y\sigma_x)$	RD′SOC
C_{4v}, C_{6v}	$\lambda_R(k_x\sigma_y - k_y\sigma_x)$	RSOC
D_2	$\lambda_D(k_x\sigma_x - k_y\sigma_y) + \lambda_W(k_x\sigma_x + k_y\sigma_y)$	DWSOC
D_4, D_6	$\lambda_W(k_x\sigma_x + k_y\sigma_y)$	WSOC
S_4	$\lambda_D(k_x\sigma_x - k_y\sigma_y) + \lambda_{D'}(k_x\sigma_y + k_y\sigma_x)$	DD′SOC
D_{2d}	$\lambda_D(k_x\sigma_x - k_y\sigma_y)$	DSOC

Figure 3. Solutions of first-principles BdG Hamiltonian demonstrate the defining TSC features of $TaSe_2$. (a) Side and top view of atomic structure. (b) Electron band structure. (c) Spin texture of the lowest band crossing the Fermi level. (d) Dispersion relation of superconducting quasi-particles. (e) Energy spectrum of quasi-particles in a 1D $TaSe_2$ nanoribbon. The chiral MEMs located at the right (left) edge are marked by the red (blue) color. (f) Distribution of Berry curvature of the pairing gap.

KPs (see Figure 3b). The system is metallic with KP located right at the Fermi level, ideal for realizing TSC as discussed above. The spin texture of the lowest band crossing the Fermi level exhibits a DSOC-type around Γ and S point (see Figure 3c), which is consistent with their little group of D_{2d}. For X and Y point, the little group of C_{2v} induces a RD′SOC-type spin texture. Similar analyses can be made for other candidates, based on Table 1 and information in Sections II and IV of the Supporting Information.

We then construct a specific BdG Hamiltonian $h_{WFs}^{BdG}(\mathbf{k})$ (see Section III of the Supporting Information) for $TaSe_2$ to demonstrate the expected TSC phase. Diagonalizing $h_{WFs}^{BdG}(\mathbf{k})$ gives the spectrum of quasi-particles (see Figure 3d), which clearly show a fully opened pairing gap at zero energy. The nontrivial gap topology was then identified by calculating the quasi-particle spectrum of one-dimensional (1D) nanoribbon (see Figure 3e). Two gapless MBMs emerge at the gap, residing on the two edges. The nontrivial topology is further confirmed by calculating Berry curvature of quasi-particle states below the gap (see Figure 3f). The Berry curvature with dominant positive values is mainly distributed near Γ, which leads to a Chern number of 1 upon integration, consistent with the MBM calculations.

The generality of our proposed theory can be further illustrated by considering a complex case of ASOC, such as antisymmetric RDD′WSOC. The RDD′WSOC is featured with an arbitrary in-plane spin texture resulting from a combination of RSOC, DSOC, D′SOC, and WSOC, which is found to evoke also a chiral TSC phase (see Section III of the Supporting Infomation). For all other candidates with diverse forms of ASOC, their TSC phase is also characterized with a nonzero Chern number of the pairing gap once the Fermi level is moved into the Zeeman gap and the condition of $\sqrt{\Delta^2 + \mu^2} < |Z|$ is satisfied.

DISCUSSION

We emphasize that the discovered TSC candidates span a wide range of crystal structures, band structures, and spin textures. First, they can have square, rectangle, and hexagonal lattices, including nearly 90 different atomic structures, each shared by abundant materials with similar chemical compositions, e.g.,

more than 80 candidates sharing the same structure with $TaSe_2$. Second, they can be metal, insulator, semiconductor, or semimetal. The metallic candidates with the KPs near the Fermi level provide opportunities for realizing intrinsic TSC without the need of doping and/or proximity effect of superconductor. Third, they exhibit diverse antisymmetric in-plane spin textures with varying compositions of RSOC, DSOC, D′SOC, and WSOC, of different SOC strength of λ_R, λ_D, $\lambda_{D'}$, and λ_W, respectively.

The physical mechanism of ASOC to trigger 2D TSC is general for the isolated KPs surrounded by in-plane spin texture, which can be realized at any TRIM for 2D materials with symmorphic SGs and with out-of-plane rotational axis. For nonsymmorphic SGs, the KPs may be connected by doubly degenerated nodal lines at edge or boundary of Brillouin zone. In this case, the remaining isolated KPs can still be exploited for realizing TSC, if they are located at different energies away from that of nodal lines. Additionally, the nodal lines may give rise to other novel superconducting state, such as the Fulde−Ferrell−Larkin−Ovchinnikov pairing state with high critical magnetic field.[50,51]

We would like to mention that the TSC phase may still be induced by ASOC with spin textures having small finite out-of-plane components. This can be inferred from the recent report of TSC phase of GeTe[31] and BiSb[32] monolayer with C_{3v} PG symmetry. The C_{3v} PG is known to give σ_z a coefficient in third-power of momentum,[46,47] which introduces an out-of-plane component in the spin texture. Despite this, the odd parity of ASOC may still evoke TSC ordering, and the nontrivial gap is not fully but "continually" opened if the pairing/Zeeman gap is small/large. Such a TSC phase can exist in other 2D materials with C_{3v}, C_3, or D_3 PG symmetry.

In a broad sense, because the odd parity of ASOC will be always maintained, a Zeeman field that breaks isolated KPs without closing pairing gap is able to evoke the TSC phase. For the in-plane spin texture discussed in this work, an out-of-plane field direction is favored for maintaining the pairing gap. When spins are orientated in out-of-plane direction by the so-called Ising SOC, an in-plane field should be applied to ensure minimum destruction of the pairing gap. This scenario of evoking TSC phases was theoretically proposed in the heavily gated MoS_2.[52,53] Given that the out-of-plane spin orientation exists in the materials with the symmetry of the listed 11 PGs (Table 1) but without the out-of-plane C_n axis, there could be more than 500 candidates (see Figure 2a) with Ising TSC in the two considered material databases.

During the preparation of this paper, we became aware of a high-throughput investigation on topological and nodal superconductors,[54] based on symmetry indicators for super-conductors.[55−59] It is interesting to note that the 2D TSC candidates we have identified here have no overlap with their database.

ASSOCIATED CONTENT

Ⓢ Supporting Information

The Supporting Information is available free of charge at https://pubs.acs.org/doi/10.1021/acs.nanolett.2c03213.

> Details and results of TB model, the little group of TRIM, details of first-principles calculations,[31,32,60−62] a list of screened 2D TSC candidates,the list of screened 2D TSC candidates, tables, and figures (PDF)

■ AUTHOR INFORMATION

Corresponding Authors

Feng Liu — *Department of Materials Science and Engineering, University of Utah, Salt Lake City, Utah 84112, United States;* ● orcid.org/0000-0002-3701-8058; Email: fliu@eng.utah.edu

Xiaoming Zhang — *College of Physics and Optoelectronic Engineering, Ocean University of China, Qingdao, Shandong 266100, China;* ● orcid.org/0000-0003-0756-9526; Email: zxm@ouc.edu.cn

Author

Jiale Liu — *College of Physics and Optoelectronic Engineering, Ocean University of China, Qingdao, Shandong 266100, China*

Complete contact information is available at:
https://pubs.acs.org/10.1021/acs.nanolett.2c03213

Author Contributions

§X.Z. and J.L. contributed equally.

Notes

The authors declare no competing financial interest.

■ REFERENCES

(1) Qi, X.-L.; Zhang, S.-C. Topological insulators and superconductors. *Rev. Mod. Phys.* **2011**, *83*, 1057−1110.

(2) Sato, M.; Ando, Y. Topological superconductors: a review. *Rep. Prog. Phys.* **2017**, *80*, 076501.

(3) Lutchyn, R. M.; Bakkers, E. P. A. M.; Kouwenhoven, L. P.; Krogstrup, P.; Marcus, C. M.; Oreg, Y. Majorana zero modes in superconductor−semiconductor heterostructures. *Nat. Rev. Mater.* **2018**, *3*, 52−68.

(4) Ivanov, D. A. Non-Abelian Statistics of Half-Quantum Vortices in *p*-Wave Superconductors. *Phys. Rev. Lett.* **2001**, *86*, 268−271.

(5) Lian, B.; Sun, X.-Q.; Vaezi, A.; Qi, X.-L.; Zhang, S.-C. Topological quantum computation based on chiral Majorana fermions. *P Natl. Acad. Sci. USA* **2018**, *115*, 10938−10942.

(6) Beenakker, C. W. J.; Baireuther, P.; Herasymenko, Y.; Adagideli, I.; Wang, L.; Akhmerov, A. R. Deterministic Creation and Braiding of Chiral Edge Vortices. *Phys. Rev. Lett.* **2019**, *122*, 146803.

(7) Nayak, C.; Simon, S. H.; Stern, A.; Freedman, M.; Das Sarma, S. Non-Abelian anyons and topological quantum computation. *Rev. Mod. Phys.* **2008**, *80*, 1083−1159.

(8) Kitaev, A. Y. Fault-tolerant quantum computation by anyons. *Ann. Phys.* **2003**, *303*, 2−30.

(9) Read, N.; Green, D. Paired states of fermions in two dimensions with breaking of parity and time-reversal symmetries and the fractional quantum Hall effect. *Phys. Rev. B* **2000**, *61*, 10267−10297.

(10) Kitaev, A. Y. Unpaired Majorana fermions in quantum wires. *Phys.-Usp.* **2001**, *44*, 131−136.

(11) Sato, M.; Takahashi, Y.; Fujimoto, S. Non-Abelian Topological Order in *s*-Wave Superfluids of Ultracold Fermionic Atoms. *Phys. Rev. Lett.* **2009**, *103*, 020401.

(12) Lutchyn, R. M.; Sau, J. D.; Das Sarma, S. Majorana Fermions and a Topological Phase Transition in Semiconductor-Superconductor Heterostructures. *Phys. Rev. Lett.* **2010**, *105*, 077001.

(13) Oreg, Y.; Refael, G.; von Oppen, F. Helical Liquids and Majorana Bound States in Quantum Wires. *Phys. Rev. Lett.* **2010**, *105*, 177002.

(14) Sau, J. D.; Lutchyn, R. M.; Tewari, S.; Das Sarma, S. Generic New Platform for Topological Quantum Computation Using Semiconductor Heterostructures. *Phys. Rev. Lett.* **2010**, *104*, 040502.

(15) Nadj-Perge, S.; Drozdov, I. K.; Li, J.; Chen, H.; Jeon, S.; Seo, J.; MacDonald, A. H.; Bernevig, B. A.; Yazdani, A. Observation of Majorana fermions in ferromagnetic atomic chains on a superconductor. *Science* **2014**, *346*, 602.

(16) Ménard, G. C.; Guissart, S.; Brun, C.; Leriche, R. T.; Trif, M.; Debontridder, F.; Demaille, D.; Roditchev, D.; Simon, P.; Cren, T. Two-dimensional topological superconductivity in Pb/Co/Si(111). *Nat. Commun.* **2017**, *8*, 2040.

(17) Kezilebieke, S.; Huda, M. N.; Vaňo, V.; Aapro, M.; Ganguli, S. C.; Silveira, O. J.; Głodzik, S.; Foster, A. S.; Ojanen, T.; Liljeroth, P. Topological superconductivity in a van der Waals heterostructure. *Nature* **2020**, *588*, 424−428.

(18) Kezilebieke, S.; Vaňo, V.; Huda, M. N.; Aapro, M.; Ganguli, S. C.; Liljeroth, P.; Lado, J. L. Moiré-Enabled Topological Superconductivity. *Nano Lett.* **2022**, *22*, 328−333.

(19) Rashba, E. I. Properties of semiconductors with an extremum loop. I. Cyclotron and combinational resonance in a magnetic field perpendicular to the plane of the loop. *Sov. Phys. Solid State* **1960**, *2*, 1109−1122.

(20) Bychkov, Y. A.; Rashba, É. I. Properties of a 2D electron gas with lifted spectral degeneracy. *JETP Letters* **1984**, *39*, 78−83.

(21) Fujimoto, S. Topological order and non-Abelian statistics in noncentrosymmetric *s*-wave superconductors. *Phys. Rev. B* **2008**, *77*, 220501.

(22) Alicea, J. Majorana fermions in a tunable semiconductor device. *Phys. Rev. B* **2010**, *81*, 125318.

(23) Schliemann, J. Colloquium: Persistent spin textures in semiconductor nanostructures. *Rev. Mod. Phys.* **2017**, *89*, 011001.

(24) Tao, L. L.; Tsymbal, E. Y. Persistent spin texture enforced by symmetry. *Nat. Commun.* **2018**, *9*, 2763.

(25) Tao, L. L.; Tsymbal, E. Y. Perspectives of spin-textured ferroelectrics. *J. Phys. D* **2021**, *54*, 113001.

(26) Hu, L.; Huang, H.; Wang, Z.; Jiang, W.; Ni, X.; Zhou, Y.; Zielasek, V.; Lagally, M. G.; Huang, B.; Liu, F. Ubiquitous Spin-Orbit Coupling in a Screw Dislocation with High Spin Coherency. *Phys. Rev. Lett.* **2018**, *121*, 066401.

(27) Li, X.; Zhang, S.; Huang, H.; Hu, L.; Liu, F.; Wang, Q. Unidirectional Spin-Orbit Interaction Induced by the Line Defect in Monolayer Transition Metal Dichalcogenides for High-Performance Devices. *Nano Lett.* **2019**, *19*, 6005−6012.

(28) Chang, G.; Wieder, B. J.; Schindler, F.; Sanchez, D. S.; Belopolski, I.; Huang, S.-M.; Singh, B.; Wu, D.; Chang, T.-R.; Neupert, T.; Xu, S.-Y.; Lin, H.; Hasan, M. Z. Topological quantum properties of chiral crystals. *Nat. Mater.* **2018**, *17*, 978−985.

(29) Xie, Y.-M.; Gao, X.-J.; Xu, X. Y.; Zhang, C.-P.; Hu, J.-X.; Gao, J. Z.; Law, K. T. Kramers nodal line metals. *Nat. Commun.* **2021**, *12*, 3064.

(30) Bihlmayer, G.; Rader, O.; Winkler, R. Focus on the Rashba effect. *New J. Phys.* **2015**, *17*, 050202.

(31) Zhang, X.; Jin, K.-H.; Mao, J.; Zhao, M.; Liu, Z.; Liu, F. Prediction of intrinsic topological superconductivity in Mn-doped GeTe monolayer from first-principles. *npj Comput. Mater.* **2021**, *7*, 44.

(32) Zhang, X.; Gao, D.; Zhu, X.; Liu, J.; Wang, W.; Liu, X.; Zhao, M. Prediction of topological superconductivity from type-IV, -III, -II, and -I′ nodal points induced by Rashba spin-orbit coupling. *Phys. Rev. B* **2021**, *104*, 245409.

(33) Chen, M.; Liu, F. Prediction of giant and ideal Rashba-type splitting in ordered alloy monolayers grown on a polar surface. *Nat. Sci. Rev.* **2021**, *8*, nwaa241.

(34) Ming, W.; Wang, Z. F.; Zhou, M.; Yoon, M.; Liu, F. Formation of Ideal Rashba States on Layered Semiconductor Surfaces Steered by Strain Engineering. *Nano Lett.* **2016**, *16*, 404−409.

(35) Dresselhaus, G. Spin-Orbit Coupling Effects in Zinc Blende Structures. *Phys. Rev.* **1955**, *100*, 580−586.

(36) Bravo, S.; Pacheco, M.; Nuñez, V.; Correa, J. D.; Chico, L. Two-dimensional Weyl points and nodal lines in pentagonal materials and their optical response. *Nanoscale* **2021**, *13*, 6117−6128.

(37) Tao, L. L.; Tsymbal, E. Y. Spin-orbit dependence of anisotropic current-induced spin polarization. *Phys. Rev. B* **2021**, *104*, 085438.

(38) Meier, L.; Salis, G.; Shorubalko, I.; Gini, E.; Schön, S.; Ensslin, K. Measurement of Rashba and Dresselhaus spin−orbit magnetic fields. *Nat. Phys.* **2007**, *3*, 650−654.

(39) Ganichev, S. D.; Bel'kov, V. V.; Golub, L. E.; Ivchenko, E. L.; Schneider, P.; Giglberger, S.; Eroms, J.; De Boeck, J.; Borghs, G.; Wegscheider, W.; Weiss, D.; Prettl, W. Experimental Separation of Rashba and Dresselhaus Spin Splittings in Semiconductor Quantum Wells. *Phys. Rev. Lett.* **2004**, *92*, 256601.

(40) He, J.; Di Sante, D.; Li, R.; Chen, X.-Q.; Rondinelli, J. M.; Franchini, C. Tunable metal-insulator transition, Rashba effect and Weyl Fermions in a relativistic charge-ordered ferroelectric oxide. *Nat. Commun.* **2018**, *9*, 492.

(41) Di Sante, D.; Barone, P.; Bertacco, R.; Picozzi, S. Electric Control of the Giant Rashba Effect in Bulk GeTe. *Adv. Mater.* **2013**, *25*, 509−513.

(42) Stroppa, A.; Di Sante, D.; Barone, P.; Bokdam, M.; Kresse, G.; Franchini, C.; Whangbo, M.-H.; Picozzi, S. Tunable ferroelectric polarization and its interplay with spin-orbit coupling in tin iodide perovskites. *Nat. Commun.* **2014**, *5*, 5900.

(43) Yamauchi, K.; Barone, P.; Shishidou, T.; Oguchi, T.; Picozzi, S. Coupling Ferroelectricity with Spin-Valley Physics in Oxide-Based Heterostructures. *Phys. Rev. Lett.* **2015**, *115*, 037602.

(44) Zhou, J.; Shen, L.; Costa, M. D.; Persson, K. A.; Ong, S. P.; Huck, P.; Lu, Y.; Ma, X.; Chen, Y.; Tang, H.; Feng, Y. P. 2DMatPedia, an open computational database of two-dimensional materials from top-down and bottom-up approaches. *Sci. Data* **2019**, *6*, 86.

(45) Gjerding, M. N.; Taghizadeh, A.; Rasmussen, A.; Ali, S.; Bertoldo, F.; Deilmann, T.; Knøsgaard, N. R.; Kruse, M.; Larsen, A. H.; Manti, S.; Pedersen, T. G.; Petralanda, U.; Skovhus, T.; Svendsen, M. K.; Mortensen, J. J.; Olsen, T.; Thygesen, K. S. Recent progress of the Computational 2D Materials Database (C2DB). *2D Mater.* **2021**, *8*, 044002.

(46) Vajna, S.; Simon, E.; Szilva, A.; Palotas, K.; Ujfalussy, B.; Szunyogh, L. Higher-order contributions to the Rashba-Bychkov effect with application to the Bi/Ag(111) surface alloy. *Phys. Rev. B* **2012**, *85*, 075404.

(47) Zhao, H. J.; Nakamura, H.; Arras, R.; Paillard, C.; Chen, P.; Gosteau, J.; Li, X.; Yang, Y.; Bellaiche, L. Purely Cubic Spin Splittings with Persistent Spin Textures. *Phys. Rev. Lett.* **2020**, *125*, 216405.

(48) Point Group Symmetry Character Tables, https://www.webqc.org/symmetry.php (09/12/2021).

(49) Elcoro, L.; Bradlyn, B.; Wang, Z.; Vergniory, M. G.; Cano, J.; Felser, C.; Bernevig, B. A.; Orobengoa, D.; de la Flor, G.; Aroyo, M. I. Double crystallographic groups and their representations on the Bilbao Crystallographic Server. *J. Appl. Crystallogr.* **2017**, *50*, 1457−1477.

(50) Zhang, X.; Liu, F. Fulde-Ferrell-Larkin-Ovchinnikov pairing induced by a Weyl nodal line in an Ising superconductor with a high critical field. *Phys. Rev. B* **2022**, *105*, 024505.

(51) Liu, C.-X. Unconventional Superconductivity in Bilayer Transition Metal Dichalcogenides. *Phys. Rev. Lett.* **2017**, *118*, 087001.

(52) Yuan, N. F. Q.; Mak, K. F.; Law, K. T. Possible Topological Superconducting Phases of MoS₂. *Phys. Rev. Lett.* **2014**, *113*, 097001.

(53) He, W.-Y.; Zhou, B. T.; He, J. J.; Yuan, N. F. Q.; Zhang, T.; Law, K. T. Magnetic field driven nodal topological superconductivity in monolayer transition metal dichalcogenides. *Commun. Phys.* **2018**, *1*, 40.

(54) Tang, F.; Ono, S.; Wan, X.; Watanabe, H. High-Throughput Investigations of Topological and Nodal Superconductors. *Phys. Rev. Lett.* **2022**, *129*, 027001.

(55) Ono, S.; Watanabe, H. Unified understanding of symmetry indicators for all internal symmetry classes. *Phys. Rev. B* **2018**, *98*, 115150.

(56) Geier, M.; Brouwer, P. W.; Trifunovic, L. Symmetry-based indicators for topological Bogoliubov-de Gennes Hamiltonians. *Phys. Rev. B* **2020**, *101*, 245128.

(57) Skurativska, A.; Neupert, T.; Fischer, M. H. Atomic limit and inversion-symmetry indicators for topological superconductors. *Phys. Rev. Research* **2020**, *2*, 013064.

(58) Ono, S.; Po, H. C.; Shiozaki, K. Z₂-enriched symmetry indicators for topological superconductors in the 1651 magnetic space groups. *Phys. Rev. Research* **2021**, *3*, 023086.

(59) Ono, S.; Shiozaki, K. Symmetry-Based Approach to Superconducting Nodes: Unification of Compatibility Conditions and Gapless Point Classifications. *Phys. Rev. X* **2022**, *12*, 011021.

(60) Kresse, G.; Furthmüller, J. Efficient iterative schemes for ab initio total-energy calculations using a plane-wave basis set. *Phys. Rev. B* **1996**, *54*, 11169−11186.

(61) Kresse, G.; Furthmüller, J. Efficiency of ab-initio total energy calculations for metals and semiconductors using a plane-wave basis set. *Comput. Mater. Sci.* **1996**, *6*, 15−50.

(62) Mostofi, A. A.; Yates, J. R.; Lee, Y.-S.; Souza, I.; Vanderbilt, D.; Marzari, N. wannier90: A tool for obtaining maximally-localised Wannier functions. *Comput. Phys. Commun.* **2008**, *178*, 685−699.

📖 Recommended by ACS